京都大学防災研究所年報 第 50 号 C 平成 19 年 4 月
Annuals of Disas. Prev. Res. Inst., Kyoto Univ., No. 50 C, 2007

Numerical Simulation of Volcanomagnetic Effects due to Hydrothermal Activity (2).

Ayako OKUBO*, Wataru KANDA and Kazuhiro ISHIHARA

*COE researcher, DPRI, Kyoto University

Synopsis

Geomagnetic field variations observed at many volcanoes suggest temperature changes and/or stress changes inside those volcanoes. Such volcanomagnetic effects are largely controlled by a behavior of volcanic fluids or hydrothermal systems that transport heat and mass from the deep source. In this study, we have developed postprocessors to calculate piezomagnetic effects caused by hydrothermal pressurization. By using a newly developed postprocessor, we carried out numerical experiments on the effect of host-rock permeability and the influence of caprock, as a factor to change the physical state within the volcanic edifice. From these evaluations, it turns out that the both effects influence not only the amount of piezomagnetic changes but also the duration of the anomalous piezomagnetic field.

Keywords: hydrothermal activity, piezomagnetic effect, numerical simulation, permeability, caprock.

1. Introduction

Continuous observations of geomagnetic total intensity have been carried out on many active volcanoes (e.g., Tanaka, 1993; Del Negro *et al*., 2004). Geomagnetic field variations observed at many volcanoes suggest temperature changes and/or stress changes, inside those volcanoes. Such volcanomagnetic effects are largely controlled by a behavior of volcanic fluids or hydrothermal systems that transport heat and mass from the deep source. Thus, volcanomagnetic effects could provide various kinds of information to understand the volcanic activity.

Recently, for the volcanomagnetic modeling of space/time changes related to hydrothermal activity, Ishido and Pritchett (2001) numerically evaluated geomagnetic field changes based on thermomagnetic effect and electrokinetic effect caused by fluid production and reinjection based on a two-dimensional geothermal reservoir model. In addition, Okubo *et al*., (2006) examined the influences of host rock permeability and depth of magma intrusion on thermomagnetic effect, and showed that the shallower depth of intrusion causes larger total intensity anomaly and earlier decline of it and that larger anomalies appear at later times in cases of lower permeability host rocks. However, in all previous work of piezomagnetic modeling, no attention has been paid to modeling of space/time changes due to hydrothermal activities. Therefore we focus on modeling for piezomagnetic effect among volcanomagnetic effects accompanied with hydrothermal activity that would be predominant in our problem.

The objective of our work is to evaluate numerically the space/time changes of piezomagnetic field associated with thermal pore-fluid pressurization. In the present study, the "HYDROTHERM version 2.2" to simulate multiphase ground-water flow and heat transport (Hayba and Ingebritsen, 1994) was used to calculate subsurface pore-fluid pressure distribution. A newly developed postprocessor was then applied to calculate piezomagnetic change based upon space/time records of underground conditions produced by the simulator. Here, the numerical simulations treated the piezomagnetic change according to a reversible phenomenon, which returns to the steady state again after increasing pressure happened temporarily under steady state, using the linear

piezomagnetic law presented by Sasai (1980). We will report results for the following cases: (1) How does the effect of host-rock permeability, which is the principal factor influencing fluid circulation in hydrothermal systems, influence the piezomagnetic changes ? (2) How does the presence of caprock influence the piezomagnetic changes ?

2. Hydrothermal Pressurization

We use the U.S. Geological Survey numerical model HYDROTHERM, version 2.2 (Hayba and Ingebritsen, 1994). The numerical model configuration, showing domain sizes, boundary and initial conditions. The configuration use 2-D axi-symmetric radial coordinates to simulate a 3-D domain (see Fig. 3). Model parameters, typical of volcanic rocks, as well as initial and boundary conditions are similar to those used by Hayba and Ingebritsen (1997). The ground surface at any point has a specified hydraulic head equal to its elevation with a constant fluid pressure of 1 *atm* and temperature of 20 ◦*C*. The right boundary, 8.5 km from the center of the edifice, maintains the initial constant pressure and temperature conditions and allows fluid and heat flow. The bottom boundary is impermeable, with a constant basal heat flux of 80 mW/m^2 into the host rock and a constant basal heat flux of 120 mW/m^2 into the pluton. The initial conditions are usually a 20 ◦*C*/km temperature gradient. As rock properties, thermal conductivity is 2 *W*/(*mK*), and solid density is 2.5 kg/m^3. Intrinsic permeability and rock heat capacity vary as functions of temperature, whereas other rock properties (porosity, density, and heat capacity) are constant throughout the simulations (Table 1). At temperature above 500 ◦*C*, we assume that the permeability of the pluton is negligibly low of $10^{-22}m^2$ (both host-rock and pluton). As temperature decreases from 500 to 400 ◦*C*, permeability increases log linearly to 10^{-19} m^2 for pluton and 10^{-17} m^2 for host-rock. As temperature decreases further to 360 ◦*C*, we assume host-rock permeabilities of 10^{-13}-10^{-15} m^2 and the pluton permeability of 10^{-18} m^2 (c.f. Manning and Ingebritsen, 1999). In addition, rock heat capacity also varies as a function of temperature. We also follow Hanson and Barton's (1989) approach as well as Hayba and Ingebritsen (1997), doubling the heat capacity of the pluton (2000*J*/(*kgK*)) for temperatures between 900◦*C* and 750◦*C*. First, simulation begins with the instantaneous intrusion of a 900 ◦*C* pluton cylinder with a radius of 0.5 *km*, and its top is 3.0 *km* beneath the ground. We also specify that initial pressure within the pluton is 10% less than lithostatic pressures. Next, after cooling pluton (300,000 years without caprock and 500,000 years with caprock), the upwelling magmatic fluid rises to the depth of 500 *m* beneath the ground from top depth of the cooling pluton for each simulation. Some models (Table2: *Models D*−*F*) include a 200*m* thick by 0.5*km* long, low-permeability horizon which represents a caprock overlying the hydrothermal system. In this study, the grid consists of 30 layers in the vertical (z) direction, and 30 blocks in the horizontal (x) direction. The x direction grid block spacing is 10m in 0m < x < 190m, 110m in 190m < x < 300m, 200m in 300m < x < 700m, 300m in 700m < x < 1000m, 500m in 1000m < x < 3000m, 1500m in 3000m < x < 6000m, 2500m in 6000m < x < 8500m. The z direction grid block spacing is 1m in 0m < z < 1m, 99m in 1m < z < 100m, 100m in 100m < z < 2000m, 250m in 2000m < z < 3500m and 500m in 3500m <z < 5000m.

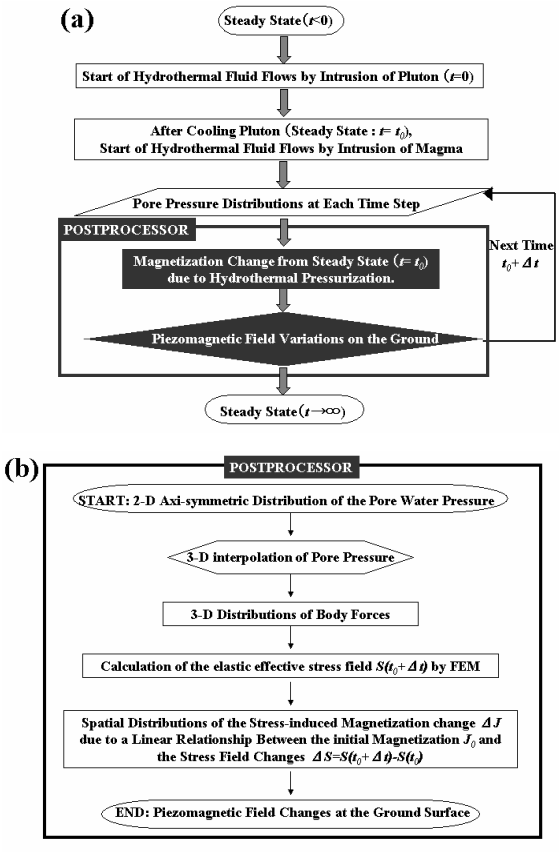

Fig. 1 The process of evaluating for piezomagnetic change in association with hydrothermal activity in this study. (a) Location of a postprocessor to the entire process. (b) Flowchart for a postprocessor.

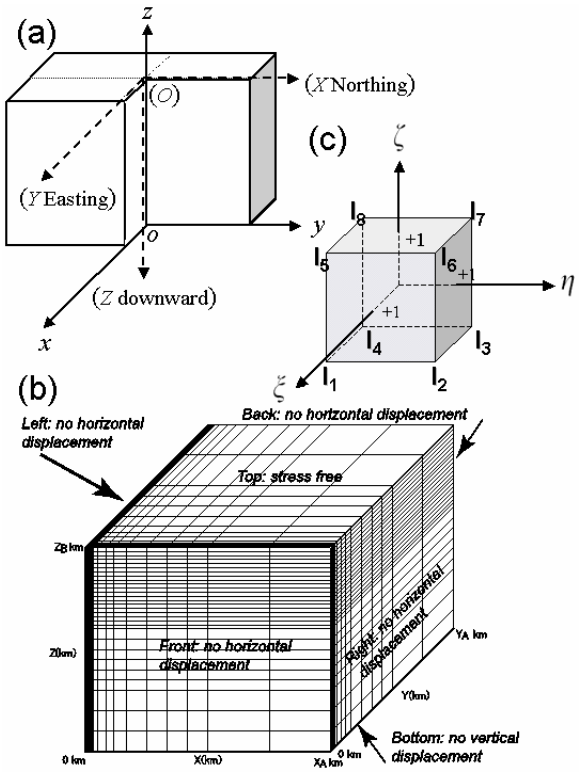

Fig. 2 The coordinate system used in this study. (a) a coordinate system (x,y,z) with origin o, which calculate effective stress field, and a coordinate system (X,Y,Z) with origin O, which calculate piezomagnetic change. (b) geometry model showing boundary and initial conditions for elastic-stress solution of the first quadrant calculated in this study. (c) a coordinate system (ξ, η, ζ) used for the element specification in the 3-D finite element method.

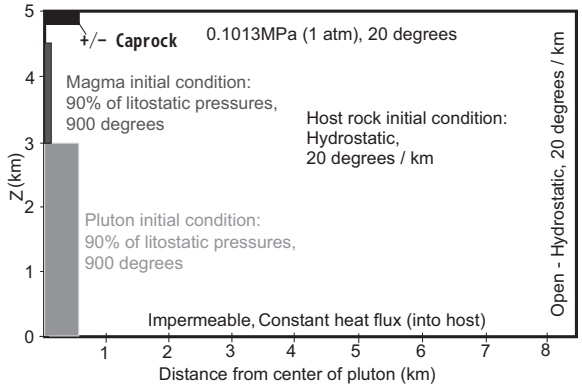

Fig. 3 Geometric model showing boundary and initial conditions for all hydrothermal fluid flow solution presented in this study.

3. The postprocessor

Displacement and stress simulations assume a linearly elastic rheology, no time-dependent stress history and no thermal stress effects according to Reid (2004). For the numerical solution of static effective-stress finite-element model, we take the Cartesian coordinate system as solid arrow shown in Fig. 2(a). For the finite-element model configuration (Fig.2b), the boundary conditions are zero horizontal displacement at the lateral margins, zero vertical displacement at the bottom boundary, and stress free (traction free) boundary at the top surface. Noted that only one quadrant was used for our calculation (see Fig. 2b), because of the symmetry of the model for hydrothermal pressurization. For the calculation of stress-induced magnetization and piezomagnetic field, we take the Cartesian coordinate system as dotted arrow shown in Fig. 2(a). The positive directions of the *X*, *Y* and *Z* axes are taken toward the geographic north, east and downward. We considered the simulation scheme as shown in Fig. 1(b) in order to estimate the piezomagnetic field changes from steady state.

Firstly, we calculated 2-D axi-symmetric hydrothermal pressurization by using a simulation code, HYDROTHERM (Ingebristen and Hayba, 1994) with various assumptions. The interpolation of 3-D pressure distribution was performed with the adjustable tension continuous curvature surface gridding algorithm (Smith and Wessel, 1990). On the basis of the simulated head distribution we then compute hydraulic gradient vector for each element by using the finite differences. This procedure is similar to that described by Iverson and Reid (1992). We determine the 3-D body forces (due to both gravity and seepage) acting on each stress node using weighted averages of the element hydraulic gradients. Secondly, we calculate the elastic effective stress field $S(t0+\Delta t)$ by using our FEM program with the body forces and appropriate boundary conditions for only one quadrant (see Fig. 1b). Thirdly, spatial distributions of the stress-induced magnetization changes ΔJ are obtained from a linear relationship between the initial magnetization $J0$ and the stress field changes $\Delta S = S(t0 + \Delta t) - S(t0)$ using eq.(1). Note that $S(t0)$ and $S(t0+\Delta t)$ indicate effective stress field for the steady state before intrusion of the magma and that for the state of *t* years after the intrusion, respectively. ΔJ of all quadrants are obtained by using the symmetry of effective stress field changes. Finally, we make use of the evaluation method proposed by Sasai and Ishikawa (1978) in order to calculate the piezomagnetic field change on the Earth's surface, and carried out case studies. The grid interval similar to hydropressure model was used to calculate the geomagnetic field change for -6000m < *x*, *y*

< 6000m and 0m <z< 5000m. It is assumed that the direction of the initial magnetization is the same as that of the geomagnetic field for each value of inclinations, I=0◦and I=90◦. In the calculation, the declination is assumed to be D=0◦.

Table 1 Rock properties used in our calculation.

Property	Pluton	Host rock	Cap rock
Permeability m^2	$f_2(T)$	$f_1(T)$	10^{-18}
Porosity %	5	10	5
Heat capacity *J/(kg K)*	*g (T)*	1000	1000
Thermal conductivity *W/(m K)*	2	2	2
Rock density kg/m^3	2500	2500	2500

4. Results and Discussions

We show how the piezomagnetic field in total intensity varies for each case of *Models A-F*, whose parameters are shown in Table 2. The amount of computer time used by the FEM program for calculating the effective stress field (total 27900 elements and 25230 nodes including both interior and surface nodes, referring to Fig. 2b) was 14400 s on Intel(R) Pentium(R) D with 3.6 GHz CPUs.

4.1 Hydrothermal Circulation, Stress-Induced Magnetization and Piezomagnetic Anomalies

Fig. 4 shows the evolving pressure and fluid-flow patterns near intrusion of the magma for Model B (Table 2). The distribution of stress-induced magnetization numerically calculated is also shown in Fig. 4. Figs. 4(a), 4(b) and 4(c) show the distribution of ΔJx for magnetization changes within the N-S cross section in the case of I = 0◦ and D = 0◦, while Figs. 4(g), 4(h) and 4(i) show the distribution of ΔJz within the N-S cross section in the case of I = 90◦ and D = 0◦. Distributions of ΔJx within the N-S cross section in the case of I = 90◦ and D = 0◦ are also shown in Figs. 4(d), 4(e) and 4(f). These figures can be regarded as ΔJz within the N-S cross section in the case of I = 0◦ and D = 0◦ and ΔJz within the E-W cross section in the case of I = 0◦ and D = 90◦. Parameters used in the calculations are listed in Table 3. The corresponding anomalies in piezomagnetic field in total intensity change are shown in Fig. 5. Figs. 5(a), 5(b) and 5(c) show piezomagnetic anomalies patterns in the case of I = 0◦ and D = 0◦, while Figs. 5(d), 5(e) and 5(f) show piezomagnetic anomalies patterns in the case of I = 90◦ and D = 0◦. The parameters assumed are the same as those listed in Table 3.

At one year after intrusion, steam appears in the upper part of the intruded magma, although flow patterns at outside of the magma are not disturbed yet by intrusion (Figs.4a, 4d and 4g). High pressure zone is restricted to the vicinity of the magma and steep gradient is seen at the interface between magma and the host. The stress-induced magnetization also shows the same tendency as the pressure. The anomalous piezomagnetic field distribution caused by high pressure magma intrusion is obtained (Figs.5a and 5d). At 32 years after the intrusion (Figs. 4b, 4e and 4f), a strong upward flow occurs at deeper part just outside of the magma. The vapor zone also extends outward as well as downwards along the interface, which results in the appearance of two-phase zone. The well-developed hydrothermal circulation is seen. However, the gradient of pressure is more gradual than that of immediately after intrusion of the magma. The amount of stress-induced magnetization is also smaller as well as the gradient of pressure. Pattern of the anomalous piezomagnetic field is similar to that obtained at 1year, although amounts of the anomaly are considerably smaller (Figs.5b and 5e). At 512 years after the intrusion, the pressure and fluid flow pattern goes to the steady state, and its stress-induced magnetization disappear (Figs.4g, 4h and 4i). The anomalous piezomagnetic fields are also disappearing (Figs.5c and 5f).

Table 2 Six models used in the case study.

Model	host rock permeability (< 360 ◦C)	Caprock
Model A	10^{-13} m^2	No present
Model B	10^{-14} m^2	No present
Model C	10^{-15} m^2	No present
Model D	10^{-13} m^2	Present
Model E	10^{-14} m^2	Present
Model F	10^{-15} m^2	Present

Table 3 Parameters of magnetic properties.

$\lambda = \mu$ Rigidity	3×10^5 bar
N Poisson's ratio	0.25
B Stress sensitivity	2×10^{-4} bar^{-1}
J_0 Initial magnetization	5.0 A/m
I Magnetic inclination	0° or 90°
D Magnetic declination	0°

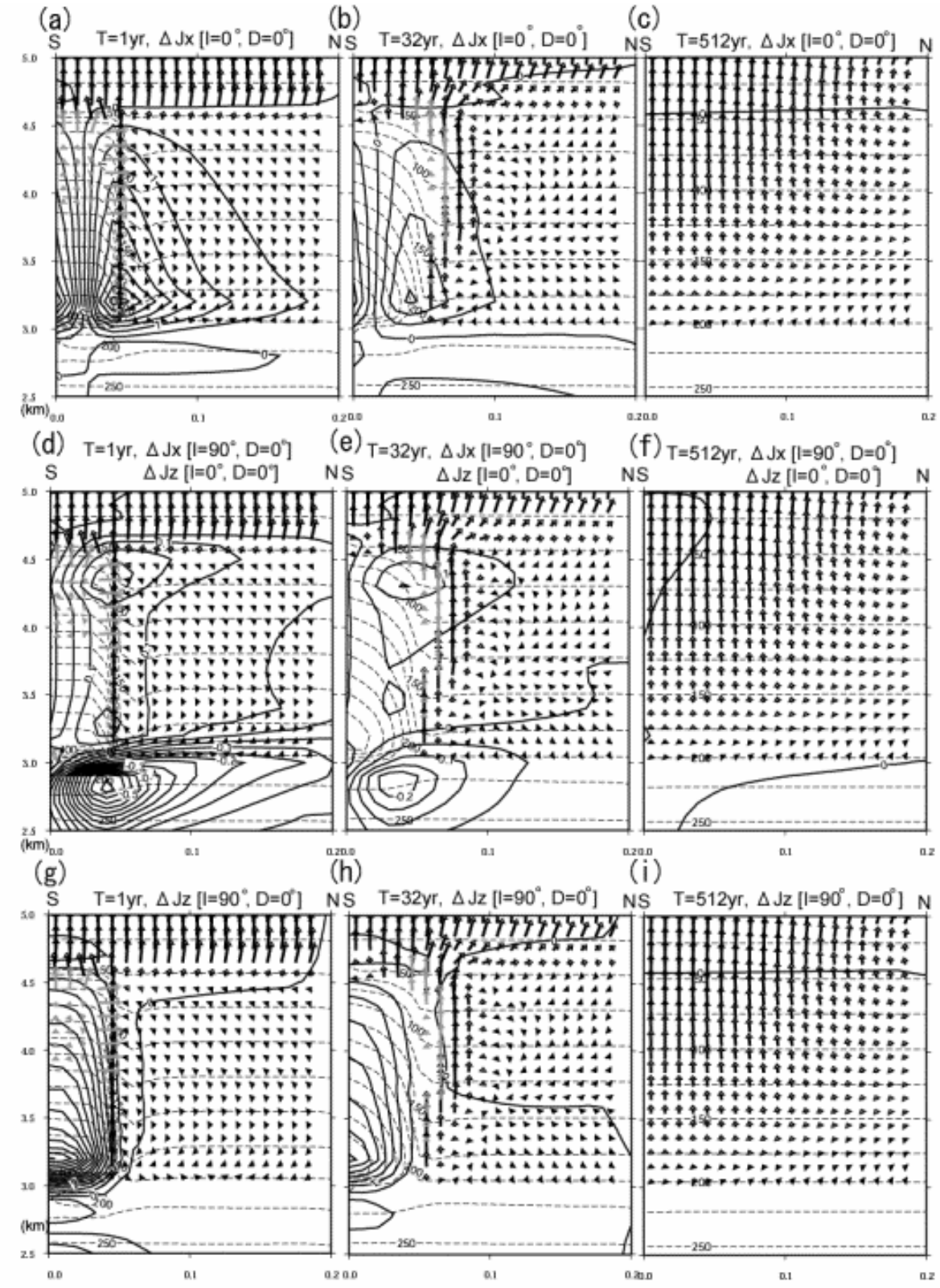

Fig. 4 Simulation results for *ModelB* showing stress-induced magnetization (solid contours), thermal pore-fluid pressurization (broken lines) and fluid-flow vectors at selected times. Solid arrows represent flow vectors for liquid and supercritical water. Shaded arrows show steam velocities and thus indicate boiling. Distributions of ΔJ_x of magnetization changes within the N-S cross section in the case of I=0◦ and D=0◦ at selected times: (a) 2^0 yr, (b) 2^5 yr and (c) 2^9 yr. Distributions of ΔJ_x of magnetization changes within the N-S cross section in the case of I=90◦ and D=0◦ at selected times: (d) 2^0 yr, (e) 2^5 yr and (f) 2^9 yr. The figures (d, e and f) also represent ΔJ_z within the N-S cross section

in the case of I=0◦ and D=0◦ and ΔJ_z within the E-W cross section in the case of I=0◦ and D=90◦. Distributions of ΔJ_z of magnetization changes within the N-S cross section in the case of I=0◦ and D=0◦ at selected times: (g) 2^0 yr, (h) 2^5 yr and (i) 2^9 yr. Unit is 10^{-5}emu/cc.

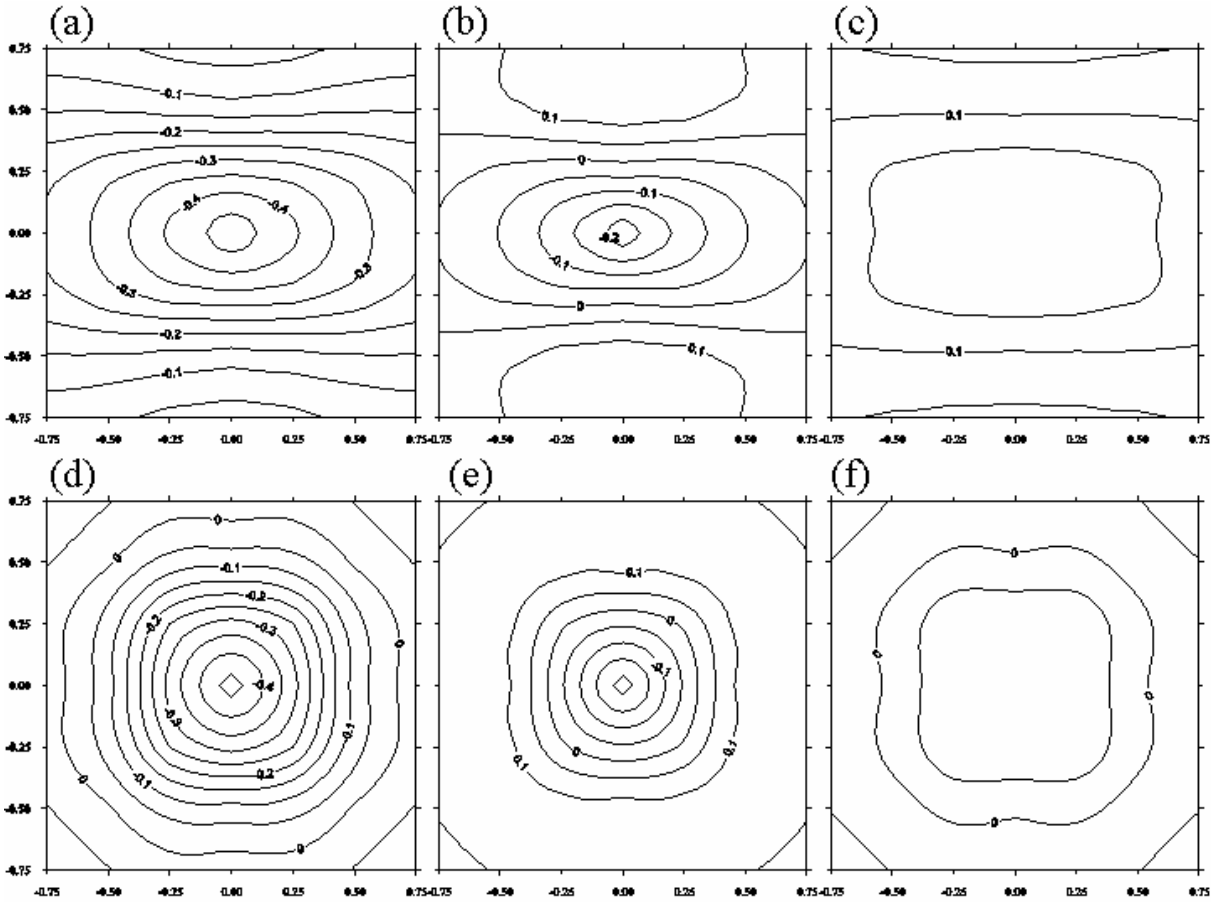

Fig. 5 Simulation results for Model B showing horizontal contour maps of calculated change in total intensity at selected times: (a) 2^0 yr, (b) 2^5 yr and (c) 2^9 yr in the case of I=0◦ and D=0◦ and (d) 2^0 yr, (e) 2^5 yr and (f) 2^9 yr in the case of I=90◦ and D=0◦. Area extends over -0.75 to +0.75 km E and -0.75 to +0.75 km N. Contour intervals show 0.05 nT.

4.2 Piezomagnetic Histories above Magma Intrusion

We summarize piezomagnetic changes in time series for the effects of host-rock permeability and caprock at the same time. The simulation shown in Figs. 6(a) and 6(b) demonstrate histories of the piezomagnetic changes at a surface point just above the center of magma intrusion, produced by the case of *I*=0◦ and *D*=0◦ and the case of *I*=90◦ and *D*=0◦, respectively. Although piezomagnetic change does not so much vary for each host-rock permeability until 1.5 year after the intrusion, less permeable already simulated larger changes from just after the intrusion. The piezomagnetic changes dramatically increase around exceeded 1.5 years after the intrusion in the case of host-rock permeabilities less than 10^{-14} m^2. In particular, the amounts of anomalies obtained by *Models E* and *F* with host-rock permeabilities of 10^{-15} m^2 reach about 10nT at 3 years after the intrusion. Generally, after exceeding 5 years, the piezomagnetic changes do not dramatically vary and gradually approach the stable state. However, there are significant differences in the amount piezomagnetic change caused by the presence or absence of a caprock after exceeding 5 years. These results suggest that the piezomagnetic changes are strongly affected by the amount and the distribution of the stress-induced magnetization caused by the effects of host-rock permeability and caprock.

5. Conclusion

We calculated spatio-temporal variations of the piezomagnetic effect caused by hydrothermal pressurization driven by the intruded magma. We utilized HYDROTHERM (Hayba and Ingebritsen, 1994)

for the fluid flow simulation after the magma intrusion and developed a postprocessor to calculate the piezomagnetic anomalies. We examined the influences of host-rock permeability and a caprock on the piezomagnetic changes. Following results were obtained in this study:

1. Host-rock permeability strongly affects both the duration of the anomalous piezomagnetic field and the amount of it. In the case of lower permeability hosts, larger anomalies maintain for a long time because thermal pressurization of pore fluid is a significant driving force for fluid flow and hydrothermal circulation is maintained in a wider area for a longer time.

2. The effect of caprock influences the amount of piezomagnetic changes. In particular, there are significant differences in the amount of piezomagnetic anomalies just above caprock, suggesting pore pressures are significantly greater in the capped system.

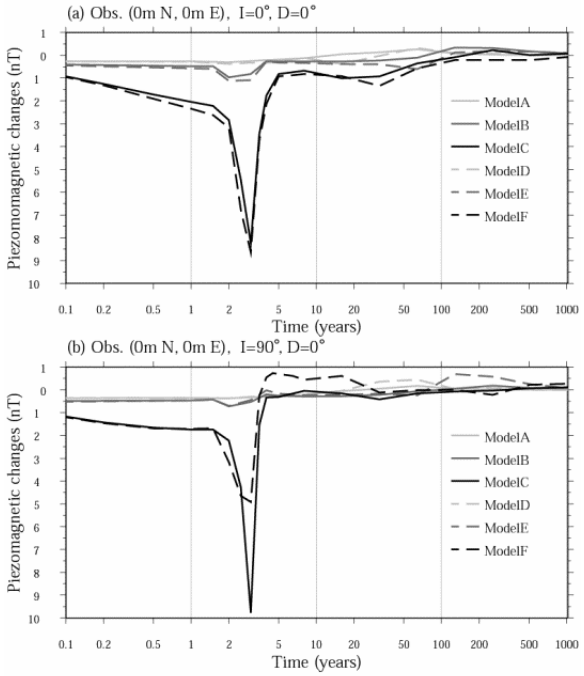

Fig. 6 Piezomagnetic histories at a surface point immediately above the center of the magma intrusion (a) in the case of I=0◦ and D=0◦ and (b) in the case of I=90 ◦and D=0◦.

Acknowledgements

The authors are grateful to Y. Sasai of, Tokyo Metropolitan Government and T. Ishido of Geological Survey of Japan for useful discussions and helpful criticism.

References

Del Negro, C. and Ferrucci, F. (2000): Volcanomagnetic effects at Vulcano Island (Aeolian archipelago, Italy), Geophys. J. Int., Vol. 140, pp. 83-94.

Hayba, D. O. and Ingebritsen, S. E. (1994): The computer model HYDROTHERM, a three-dimensional finite-difference model to simulate ground-water flow and heat transport in the temperature range of 0 to 1,200 ◦C, U. S. Geol. Surv. Water Resour. Invest. Rep., No. 94-4045, 85 pp.

Hayba, D. O. and Ingebritsen, S. E. (1997): Multiphase groundwater flow near cooling plutons, J. Geophys. Res., Vol. 102, pp. 12235-12252.

Ishido, T. and Pritchett J. W. (2001): Prediction of magnetic field changes induced by geothermal fluid production and reinjection, GRC Transactions, Vol. 25, pp. 645-649.

Manning, C. E. and Ingebritsen, S. E. (1999): Permeability of the continental crust: Implications of geothermal data and metamorphic systems, Rev. Geophys., Vol. 37, pp. 127-150.

Okubo, A., Kanda, W., and Ishiara, K. (2006): Numerical Simulation of Volcanomagnetic Effects due to Hydrothermal Activity. Annuals of Disas. Prev. Res. Inst., Kyoto Univ., Vol. 49(C), pp. 211-218.

Reid, M. E., (2004): Massive collapse of volcano edifices triggered by hydrothermal pressurization. Geology, Vol. 32, pp. 373-376.

Sasai, Y. and Ishikawa, Y. (1978): Changes in the geomagnetic total force intensity associated with the anomalous crustal activity in the Eastern part of the Izu Peninsula (2) － the Izu-Oshima-Kinkai earthquake of 1978 －, Bull. Earthq. Res. Inst., Univ Tokyo, Vol. 53, pp. 893-923.

Sasai, Y. (1980): Application of the elasticity theory of dislocations to tectonomagnetic modeling, Bull. Earthq. Res. Inst., Univ Tokyo, Vol. 55, pp. 387-447 (in Japanese with English abstract).

Tanaka, Y. (1993): Eruption mechanism as inferred from geomagnetic changes with special attention to the 1989-1990 activity of Aso volcano, J. Volcanol. Geotherm. Res., Vol. 56, pp. 319-338.

熱水流動を考慮した火山地磁気効果の数値シミュレーション（２）

大久保綾子*・神田径・石原和弘

＊ 京都大学防災研究所COE研究員

要旨

マグマ貫入後の熱水流動のシミュレーションを行い，熱水系の消長によって地表でのピエゾ磁場がどのように変化するかを数値的に評価した。シミュレーションで得られる間隙水圧の分布から火山体内部の磁化変化分布を見積もり，地表でのピエゾ磁気変化を計算するポストプロセッサを開発し，浸透率および不透水岩体であるキャップロックがピエゾ磁気変化にどの程度影響を与えるかをケーススタディ化することで調べた。その結果，浸透率が小さい方が，地磁気変化が大きく，地磁気変化が観測される時間が長いこと，またキャップロックが存在する場合は，存在しない場合と比べて地磁気変化が大きくなることがわかった。

キーワード: 熱水流動，ピエゾ磁気効果，シミュレーション，マグマ貫入，浸透率，キャップロック